Analysis of diamond nanocrystal formation from multiwalled carbon nanotubes

Andre R. Muniz,[1] Tejinder Singh,[1] Eray S. Aydil,[2] and Dimitrios Maroudas[1,*]
[1]*Department of Chemical Engineering, University of Massachusetts, Amherst, Massachusetts 01003-3110, USA*
[2]*Department of Chemical Engineering and Materials Science, University of Minnesota, Minneapolis, Minnesota 55455, USA*
(Received 3 July 2009; revised manuscript received 25 August 2009; published 8 October 2009)

A systematic analysis is presented of the nanocrystalline structures generated due to the intershell C-C bonding between adjacent concentric graphene walls of multiwalled carbon nanotubes (MWCNTs). The analysis combines a comprehensive exploration of the entire parameter space determined by the geometrical characteristics of the individual graphene walls comprising the MWCNT with first-principles density-functional theory calculations of intershell C-C bonding and structural relaxation by molecular-dynamics simulation of the resulting nanocrystalline structures. We find that these structures can provide seeds for the nucleation of the cubic-diamond and hexagonal-diamond phase in the form of nanocrystals embedded in the MWCNTs. The resulting lattice structure is determined by the chirality and relative alignment of adjacent graphene walls in the MWCNT. These crystalline phases are formed over the broadest range of nanotube diameters and for any possible combination of zigzag, armchair, or chiral configurations of graphene walls. The key parameter that determines the size of the generated nanocrystals is the chiral-angle difference between adjacent graphene walls in the MWCNT.

DOI: 10.1103/PhysRevB.80.144105 PACS number(s): 61.48.De, 64.70.Nd, 61.46.Fg, 61.46.Hk

I. INTRODUCTION

Hybridization between *s* and *p* orbitals in carbon allows it to form a variety of allotropes such as cubic diamond, hexagonal diamond (lonsdaleite),[1,2] graphite, and fullerenes.[3,4] Graphite is the most stable allotrope at ambient conditions while naturally occurring cubic diamond is formed at high pressures and temperatures present deep within the earth or through a yet unknown process in interstellar space.[5,6] Diamond can also be synthesized by compressing graphite to high pressures,[7,8] irradiating graphitic carbon with ion or electron beams,[9–11] thermal activation of graphite,[12] or through vacuum plasma deposition from methane and hydrogen at high temperatures.[13] In fact, reactions responsible for the deposition of diamond thin films have been implicated as a possible mechanism for the formation of interstellar diamond dust.[14] Lonsdaleite was first discovered in meteorites and is thought to have formed from graphite by shock compression during terrestrial impact, though formation through direct crystallization in space before entry into the earth's atmosphere has also been suggested.[1,2,15] In addition to these familiar allotropes, carbon has been reported to exist in two yet unsolved but presumably cubic structures, commonly referred to as *n*-diamond and *i*-carbon.[7,16,17] Diffraction evidence for these phases is encountered in carbonaceous materials made by shock compression of graphite or by plasma-assisted deposition of thin films from hydrocarbon and H containing electrical discharges.[7,16,18,19]

Hydrogen atoms play a critical role in determining the crystallinity of group-IV materials grown by plasma deposition. For example, nucleation and growth of diamond thin films by plasma deposition from hydrocarbons is possible only when the feed gases are heavily diluted in H_2 or under conditions where atomic H is present in copious amounts.[13,20] Another example is the amorphous-to-nanocrystalline transformation of hydrogenated silicon thin films upon exposure to H atoms from a H_2 plasma.[21–23] Furthermore, nanometer-size diamonds have been formed from multiwalled carbon nanotubes (MWCNTs) and carbon onions by exposure to H atoms from a H_2 plasma or electron-beam exposure at or above 1000 K;[9,24,25] interactions of H atoms with MWCNTs have been speculated to be responsible for the transformation of MWCNT walls to diamond nanocrystals.[24] The underlying mechanism of the H-induced structural transition in MWCNTs leading to nanocrystalline carbon is not well understood. However, several possible mechanisms for this transition have been proposed, such as the formation of H-induced sp^3 defects in carbon nanotube walls with implications for formation of nanocrystalline carbon.[26] The interactions of H atoms with the graphene walls of MWCNTs can trigger $sp^2 \rightarrow sp^3$ C-C bonding transitions. These sp^3-bonded local structures induced by hydrogen atoms or electron irradiation in MWCNTs can promote intershell C-C bonding and have been implicated to enhance material properties of MWCNTs.[27,28]

The stability of diamond nanocrystals and its size dependence has been discussed extensively in the literature;[29–32] specifically, diamond nanocrystals have been shown to be the most stable phase of carbon at the nanoscale for clusters with diameters ranging from ~1.9 to ~5.2 nm.[32] The stability of the one-dimensional equivalent nanostructures, namely, diamond nanowires, both monolithic and in the form of hollow cylinders, also has been investigated thoroughly.[33–37] It has been demonstrated that the stability of these nanowires is a function of their diameter, their surface morphology, as well as the crystallographic direction of their principal axes. The above-mentioned studies refer to isolated nanocrystals[29–32] or practically infinitely long diamond nanowires.[33–37] Here, we focus on the formation of diamond nanostructures consisting of diamond nanocrystals embedded into MWCNTs.

The purpose of this paper is to analyze the structures generated as a result of the intershell C-C bonding of adjacent, concentric graphene walls of MWCNTs. We demonstrate that these structures can provide seeds for the nucleation of cubic- and hexagonal-diamond nanocrystals and that the

chirality and relative alignment of the adjacent MWCNT graphene walls determine the lattice structure of the resulting crystalline phase. In addition, we show that the formation of diamond nanocrystals is possible over the broadest range of nanotube diameters and through any arrangement of adjacent graphene walls, i.e., for all possible combinations of zigzag, armchair, or chiral graphene wall configurations to within a certain range of the difference in the chiral angles between adjacent graphene walls in the MWCNT.

The paper is structured as follows. Section II outlines the computational methods employed in our analysis of intershell C-C bonding in MWCNTs, including first-principles density-functional theory (DFT) calculations and structural relaxation based on molecular-dynamics (MD) simulation. In Sec. III, the results of our analysis are presented and discussed. In Sec. III A, a systematic presentation is given of all the relevant geometrical aspects of C-C bond formation between adjacent concentric graphene walls by spanning the entire space of geometrical parameters as determined by the indices (m,n) (Ref. 38) of the individual nanotubes involved; our DFT calculations of intershell C-C bonding in MWCNTs and analysis of the resulting relaxed structures are presented in Sec. III B; our MD computations of structurally relaxed seeds for nucleation of crystalline carbon phases through intershell C-C bonding in MWCNTs are presented in Sec. III C. Finally, the main conclusions of our study are summarized in Sec. IV.

II. COMPUTATIONAL METHODS

The first step in our analysis consists of a general, systematic geometrical study of adjacent concentric graphene walls in MWCNTs focusing on the range of possibilities for intershell C-C bonding and its implications for the crystalline structures that can be nucleated through such a process; this is presented in Sec. III A. Subsequently, we use a synergistic combination of MD simulations with first-principles DFT calculations in order to relax fully and characterize in detail the nanostructures that can be nucleated as a result of such bond formation.

First-principles DFT calculations[39,40] were conducted within the generalized gradient approximation,[41] employing the supercell approximation, ultrasoft pseudopotentials,[42] and plane-wave basis sets[43] as implemented in the commercial code VASP.[44] This level of theoretical calculations was used for the study of intershell interactions and C-C bonding between adjacent graphene walls in MWCNTs, as well as the detailed analysis of bulk crystalline carbon phases. The results of intershell C-C bonding reported in Sec. III B are based on DFT calculations that employed a supercell consisting of 180 C atoms arranged to form three concentric CNTs with indices (6,0), (15,0), and (24,0), i.e., a (6,0)@(15,0)@(24,0) CNT configuration, a vacuum region between neighboring (periodic-image) MWCNTs that was at least 15 Å in thickness, and continuity in the axial direction. In addition, we conducted DFT calculations of intershell C-C bonding and the formation of nanocrystalline seeds for nucleation of the cubic-diamond and hexagonal-diamond (lonsdaleite) phases in CNTs of larger diameters up to 1.4 nm and confirmed that the curvature effects were minimal on the outcome of this analysis. In particular, for concentric CNTs with indices (6,0)@(15,0) and (18,0)@(27,0), with spacing between the CNT walls of 3.53 Å, nuclei for crystalline carbon phases were generated as well through intershell C-C bonding.

The results reported in Sec. III B are based on DFT calculations with a kinetic-energy cutoff of 350 eV and two **k** points in the relevant irreducible wedge of the first Brillouin zone. To calculate the total energies of the geometrically optimized configurations, the supercell was relaxed using a conjugate gradient algorithm until the differences in electronic and ionic self-consistent energies were lower than 10^{-3} and 10^{-2} eV, respectively. For DFT calculations of bulk carbon structures, a kinetic-energy cutoff of 550 eV was used and **k**-point sampling for each structure was carried out using a $16\times16\times16$ Monkhorst-Pack grid.[45] The corresponding optimal lattice parameters were determined by supercell edge size relaxation calculations. In all of our DFT calculations, systematic convergence tests were conducted (with respect to supercell size, kinetic-energy cutoff, and **k**-point grid resolution) in order to guarantee the precision of the reported results. In both MWCNTs with intershell C-C bonding and bulk crystalline carbon phases, the local bonding environment also was analyzed by visualizing planar sections of the three-dimensional valence electron-density distribution.

In our MD simulations of intershell C-C bonding and accompanying structural relaxation, the interatomic interactions were described by the adaptive intermolecular reactive empirical bonding order (AIREBO) potential.[46] AIREBO is a modified version of Brenner's reactive empirical bonding order potential[47,48] and has been used in previous studies for modeling solid carbon and hydrocarbon molecules.[46,49] In the MD simulations, the classical equations of motion were integrated using a leapfrog Verlet algorithm and time-step sizes of approximately 1.0 fs. All the MD simulations were conducted at constant temperature and (zero) pressure using the Berendsen thermostat and barostat[50] for temperature and pressure control. In our MD computations of intershell C-C bonding, periodic boundary conditions were applied in the axial direction of the CNTs. Periodic boundary conditions in all three directions (i.e., bulk supercells) were employed for MD computations in bulk crystalline phases.

We have tested and validated the AIREBO potential predictions extensively for their quantitative accuracy through comparisons with first-principles DFT calculations for the structure and properties of bulk crystalline carbon phases, as well as for chemisorption of H atoms on CNTs.[26,51,52] Some representative results from this comparative study are shown in Table I, where our AIREBO-MD and our first-principles DFT predictions for the lattice parameters and cohesive energies of crystalline carbon phases are compared. In addition, we have carried out systematic comparisons between our AIREBO-MD predictions of fully relaxed structures resulting from intershell C-C bonding in MWCNTs and the corresponding predictions of our DFT calculations for the same MWCNT configurations. In general, the AIREBO predictions are in excellent qualitative agreement and in very good quantitative agreement with the DFT calculations; the agreement is excellent in comparing overall structure, average

TABLE I. Comparison between AIREBO and first-principles DFT predictions of the equilibrium lattice parameters and cohesive energies of the cubic-diamond, hexagonal-diamond (lonsdaleite), and graphite crystalline phases. The cohesive energy differences given in parentheses are expressed with respect to the cohesive energy of graphite. Comparisons of the lattice-parameter predictions and predictions of the cohesive-energy ordering (relative stability between phases) confirms good agreement between AIREBO and DFT in describing bulk crystalline carbon phases.

	Equilibrium lattice parameter (Å)		Cohesive energy (eV)	
Phase (Space group)	DFT	AIREBO	DFT	AIREBO
Graphite ($P6_3/mmc$,194)	a=2.46, c=3.40	a=2.43, c=3.40	9.05(0.00)	7.45(0.00)
Diamond ($Fd\bar{3}m$,227)	a=3.57	a=3.57	8.92(0.13)	7.39(0.06)
Lonsdaleite ($P6_3/mmc$,194)	a=2.52, c=4.12	a=2.52, c=4.11	8.89(0.16)	7.24(0.21)

bond lengths and bond angles, and energetic ordering (relative stability) of crystalline phases and it is very good in comparing lattice parameters, individual bond lengths and bond angles, and energy differences between crystalline phases.

III. RESULTS AND DISCUSSION

A. Geometrical parameters controlling C-C bonding between adjacent graphene walls of MWCNTs

First, we conducted a systematic geometrical analysis to map out the range of possibilities for intershell C-C bonding and considered the implications of such bonding for the resulting crystalline structures. Such a geometrical analysis provides general fundamental principles for the possible atomic structures that may be formed through intershell C-C bonding, regardless of the level of theory involved in the description of interatomic interactions. This generality can be achieved by spanning the space of parameters responsible for the geometrical features of each individual, concentric nanotube in the MWCNT; this parameter space is determined by each individual nanotube's indices (m,n). The only constraint in this geometrical analysis is that the spacing between adjacent nanotubes in the MWCNT is kept at ~3.4 Å; this intertube spacing is consistent with experimentally measured distances between adjacent graphene walls in MWCNTs, as well as between parallel graphene sheets.[53]

Initially, we consider such geometrical possibilities by examining parallel planar sheets of graphene and then generalize the analysis to the curved space of MWCNTs. Figure 1 shows three possible alignments between two adjacent graphene planes together with the relaxed structures generated, in each case of alignment, by the formation of interplanar C-C bonds; how the structural relaxation has been carried out (i.e., from first principles or according to an empirical force field) is of secondary importance for this discussion. In the configuration of Fig. 1(a), the relative positions of the hexagonal cells of each plane show that the two graphene planes are displaced with respect to each other in the y direction of a Cartesian frame of reference by a distance equal to one side length of the regular hexagon; these hexagonal cells correspond to graphene six-member rings consisting of sp^2-bonded C atoms and the side of the regular hexagon has length equal to the sp^2 C-C bond length. In the configuration of Fig. 1(b), the hexagonal cells of the two parallel graphene planes overlap fully when projected onto the same (x,y) plane normal to the z direction. In the configuration of Fig. 1(c), the two graphene planes are displaced with respect to each other in the y direction by one half of the sp^2 C-C bond length. In the bonded configurations shown in Figs. 1(a) and 1(b), the C-C bonds form in the z direction between interplanar nearest neighbors. In Fig. 1(a), the interplanar bonded region resembles closely the structure of the cubic-diamond phase and can be viewed as a seed unit for the nucleation of this phase from interacting graphene planes. In contrast, the interplanar bonded region of Figs. 1(b) and 1(c) resemble the structure of the hexagonal-diamond phase (lonsdaleite) and can be viewed as seed units for hexagonal-diamond formation due to the interplanar interactions of parallel graphene sheets.

Compared to the case of parallel graphene planes, the number of geometrical possibilities is much larger in MWCNTs. Specifically, in a MWCNT, for a given pair of adjacent concentric graphene walls of given chiralities, it is possible to find regions characterized by each one of the relative alignments depicted in Fig. 1. Consequently, in the same MWCNT, different types of local crystalline structures may be generated due to intershell C-C bonding, depending on the local alignment of the graphene walls at the sites

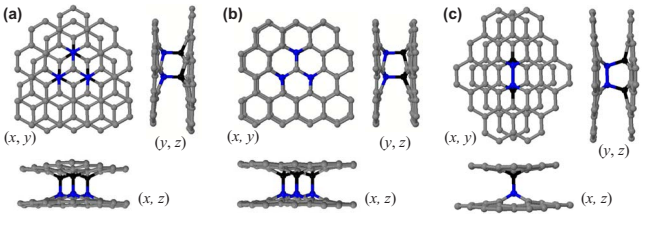

FIG. 1. (Color online) Three possible alignments, (a), (b), and (c), between two adjacent graphene planes and respective local structures generated by the formation of interplanar C–C bonds. In each case, different planar views are displayed in a Cartesian frame of reference. Dark gray (blue online) and black spheres are used to denote C atoms on the two adjacent graphene planes, respectively, that are bonded to each other.

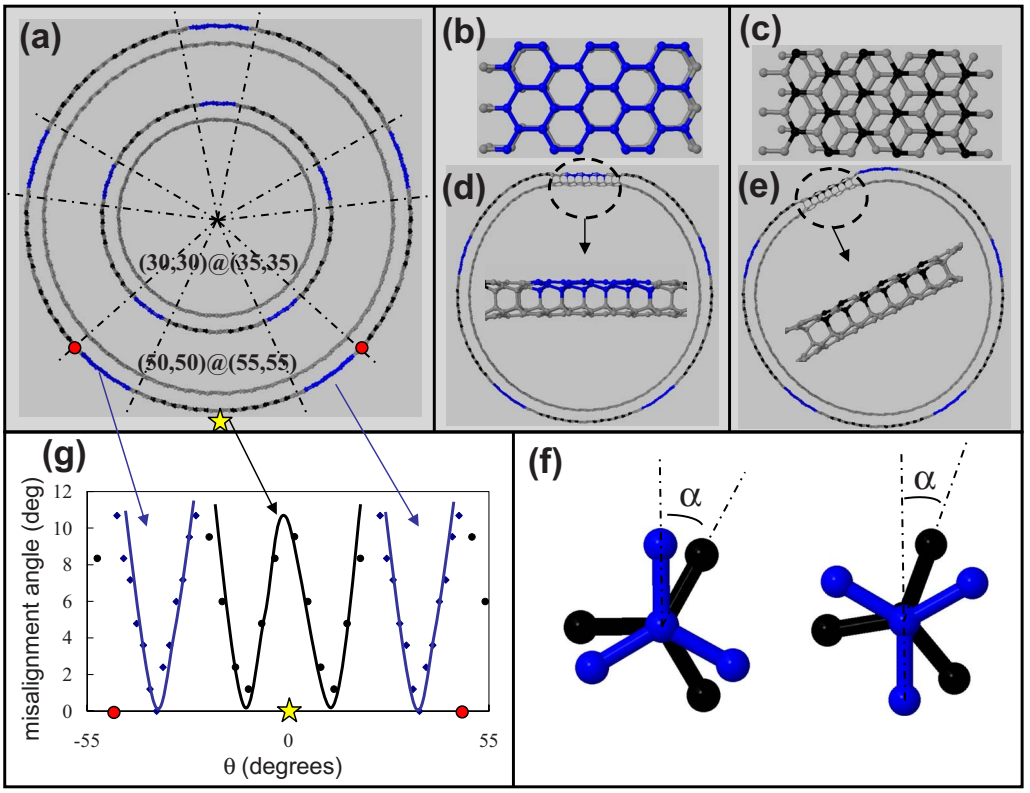

FIG. 2. (Color online) (a) Top view of relative alignment maps for two pairs of armchair nanotubes, (30,30)@(35,35) and (50,50)@(55,55), arranged concentrically. The dotted lines are used to mark the regions (a total of ten) where a certain alignment, type I or type II, is favored. [(b) and (c)] Front views of the (50,50)@(55,55) DWCNT in (b) a region where type-II alignment is favorable and (c) a region where type-I alignment is favorable. [(d) and (e)] Top views of the (50,50)@(55,55) DWCNT with close views of the local structures generated by intershell C-C bond formation in (d) one of the regions shaded dark gray (colored blue online) in (a) where type-II alignment is favorable and (e) one of the regions colored black in (a) where type-I alignment is favorable. (f) Angle α used for determining the possible alignment type according to the criteria described in the text. (g) Misalignment angle between nearest-neighbor atoms in different adjacent concentric nanotube graphene walls as a function of the polar angle θ in a cylindrical frame of reference for the sections marked in (a).

bridged by the intershell C-C bonds; these structures may grow to form nanocrystals separated by phase boundaries. For illustration purposes, we consider the simplest possible case, namely, double-walled CNTs (DWCNTs) with two concentric graphene walls of the same chirality.

To identify the type of local crystalline structure that is the most likely to be formed in a certain region of the DWCNT around a chosen point at the outer graphene wall, we use images that represent "relative alignment maps;" for a given pair of nanotube walls, these maps depict the regions of the DWCNT where a certain relative alignment between the walls is found according to detailed geometrical criteria. Figure 2(a) shows the top view of such a relative alignment map for two pairs of armchair nanotubes arranged concentrically; a larger one, (50,50)@(55,55), and a smaller one, (30,30)@(35,35). In each of these pairs of nanotubes, the alignments of the atoms marked in black and dark gray (blue online) with respect to their nearest neighbors in the adjacent nanotube are consistent with those depicted in Figs. 1(a) and 1(b), respectively, for neighboring atoms between adjacent graphene planes; these are denoted as type-I and type-II alignment, respectively. It is evident that the same type of relative alignment can be found in different regions of the nanotube. For the case under consideration, the clusters of atoms with the same relative alignment with respect to their neighbors in the adjacent nanotube have a finite size in the θ direction and an infinite size along the nanotube axis (i.e., limited by the actual CNT length); θ is the polar angle in a cylindrical-coordinate description of the CNTs, ranging from 0 to 2π, with the nanotube axis taken along the z direction. Figures 2(b) and 2(c) show close planar views for two distinct regions of the DWCNT, highlighting the two different types (II and I, respectively) of relative alignment.

Figure 2(a) also shows that the clusters of atoms with each type of relative alignment between graphene walls occur periodically as the circumference of the DWCNT is spanned along θ. For a pair of armchair nanotubes, there are five regions with type-I alignment and five regions with type-II alignment in a pattern of alternating alignment type (…I-II-I-II…). In a MWCNT, this number of regions is the same for any pair of adjacent armchair nanotubes, which satisfies the requirement of having an intertube spacing of ~3.4 Å; for concentric armchair configurations, this spacing corresponds to combinations of $(n,n)@(n+5,n+5)$ graphene walls. As the diameter of the nanotube increases, the size of each individual region (cluster of atoms with

given-type alignment) also increases; however, the number of such regions remains always the same. This trend is evident in Fig. 2(a).

Figures 2(d) and 2(e) depict the local structures resulting from the creation of intershell C-C bonds in two different regions among the ten ones shown in Fig. 2(a) for the (50,50)@(55,55) DWCNT; these structures have been relaxed after bonding using AIREBO MD. The intershell bonded structure of Fig. 2(d) corresponds to a type-II alignment and resembles the lattice structure of the hexagonal-diamond phase while that of Fig. 2(e) corresponds to a type-I alignment and resembles the lattice structure of the cubic-diamond phase.

Analogous patterns also occur in pairs of adjacent zigzag graphene walls. However, in such an arrangement of nanotubes, there are nine regions with specific alignment in a pattern of alternating alignment types (as opposed to five in the case of armchair graphene walls discussed above). This is the case for any pair of adjacent zigzag nanotubes in a MWCNT where the intertube spacing is ~3.4 Å; for concentric zigzag configurations, this spacing corresponds to combinations of $(n,0)@(n+9,0)$ graphene walls.

It should be emphasized that, over the extent of each region marked in the relative alignment maps, the relative alignment between the adjacent graphene walls is not as perfect as depicted in the planar geometry of Fig. 1. There may be slight deviations from the ideal alignment of each type, which still facilitate the formation of the corresponding intershell bonded local structures. To determine the relative alignment type that is most suitable for a given atom on a wall of the DWCNT, we used two criteria. To apply the first criterion, we find the atom in the outer layer that is the closest to a given atom in the inner layer, as well as the relative orientation of the (three) sp^2 C-C bonds formed by each one of these atoms in the individual nanotubes. If the sp^2 bonds in one graphene wall are parallel to those in the other wall and point (outwards from the atom under consideration) to the same direction, a type-II alignment is favored; on the other hand, if the sp^2 bonds in the two graphene walls are parallel but point to opposite directions, a type-I alignment is favored. A tolerance must be prescribed in assessing the bonds as being "parallel." Structural relaxations on bonded graphene planes showed that deviations from being parallel up to angles $\alpha=30°$ allow the formation of interplanar C-C bonds; this angle α is depicted in Fig. 2(f) for both types of alignment. The second necessary criterion is derived from the angle β formed between the line connecting the intershell nearest-neighbor pair of atoms and the projection of the atom of the inner layer on the outer one along the radial direction, which is used as a metric for the degree of alignment. For two perfectly aligned points, the aforementioned projected point and the nearest-neighbor atom in the outer layer coincide and $\beta=0$. By analyzing the relative alignment of atoms for two graphene walls of the same chirality, we can define a maximum misalignment angle that determines the preference for a certain type of relative alignment. This critical value corresponds to an atom of the inner graphene wall that forms the same angle with two different neighboring atoms of the outer graphene wall, with each one resulting in a different type of alignment (I or II) after intershell bonding. Figure 2(g) shows the dependence of this misalignment angle on the polar coordinate θ of the atoms on the outer nanotube; the star marked in Fig. 2(a) corresponds to $\theta=0°$. Three curves are identified in the plot of Fig. 2(g) corresponding to the regions marked in Fig. 2(a). The central atom of each blue region in the outer tube is aligned perfectly with an atom in the inner tube (a misalignment angle of 0°), corresponding to the minimum of each blue curve. The misalignment angle increases as θ changes from its value at that central point, until the type of alignment changes. For the black regions, the plotted curve exhibits two minima, corresponding to two regions of the same alignment connected to each other with a maximum (essentially a discontinuity) at the middle point.

One important point that should be considered is that, in an actual MWCNT, two adjacent graphene walls do not necessarily have the same chirality. It has been observed experimentally that there is no correlation between the chiral angles, χ, of adjacent graphene walls in MWCNTs;[54] in addition, the difference between the chiral angles of each nanotube can range from small to large values. However, we can show that it is possible to find the same types of relative alignment discussed above for pairs of graphene walls of different chiralities, provided that the difference in the chiral angle between the two walls, $\Delta\chi \equiv |\chi_{\text{inner}} - \chi_{\text{outer}}|$, is not too large.

At this point, it is worth pointing out the analogy between our relative alignment maps and the concept of the Moiré pattern that results from the rotation of one graphene plane with respect to another: this leads to a new periodic structure that has the same symmetry with the original hexagonal lattice, but a larger periodicity; the observation of superlattices on graphite in scanning tunneling microscopy images[55–58] has been attributed to such Moiré patterns. The unit cells of these Moiré patterns have been shown to correspond to domains of the structure with a certain type of stacking of two subsequent planes.[56,57] In other words, if two adjacent graphene planes are rotationally misoriented, the three types of alignment depicted in Fig. 1 will be present in the structure. In order to find the size and distribution of the regions with a desired alignment throughout the DWCNT, relative alignment maps analogous to those depicted in Fig. 2(a) were generated for a broad range of combinations of graphene walls, using the criteria defined before.

It must be mentioned that the periodicity of the resulting Moiré superperiodic lattice, D, is related to the periodicity of the original hexagonal lattice, d, by the expression $D = d/[2\sin(\phi/2)]$, where ϕ is the rotation angle. In the case of DWCNTs, ϕ corresponds to the difference in the chiral angles between the adjacent layers, $\Delta\chi$. The Moiré pattern periodicity, D, can be related to the size of the resulting domains with a certain relative alignment for a given value of $\Delta\chi$. However, in the curved space of CNTs, a direct application of this rule is not trivial in the sense that quantitative differences arise in different cases (different tube diameters, chiralities, and misalignment angle variations). Consequently, in our analysis, we relied on numerical determination of the relative alignment maps and the sizes of the resulting domains/clusters following the same methodology employed in the case where two adjacent walls have the same chirality (analogous to aligned planes or $\phi=0$).

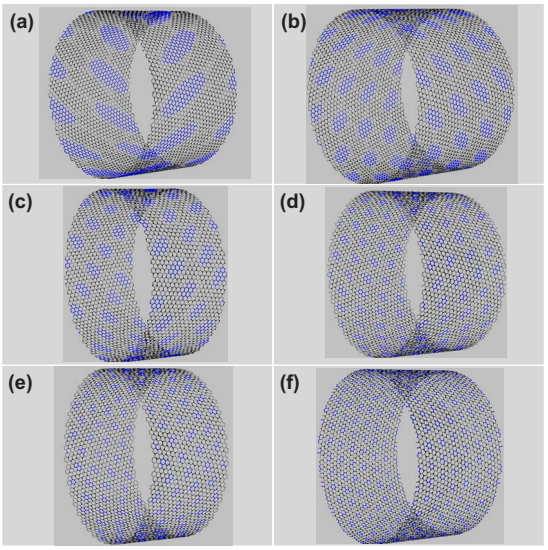

FIG. 3. (Color online) Relative alignment maps for DWCNTs formed by two chiral nanotubes with a difference in the chiral angles, $\Delta\chi$, varying from 3.88° to 16.8° and an average diameter, D, of approximately 8.9 nm. The dark gray (blue online) and black colored regions correspond to atoms with intershell alignments as depicted in Figs. 1(a) and 1(b), respectively, which favor the formation of hexagonal-diamond and cubic-diamond seeds, respectively. Only the outer nanotubes are shown for clarity. The DWCNTs have indices (a) (87,29)@(88,40) with D=8.88 nm and $\Delta\chi$=3.89°; (b) (80,40)@(98,28) with D=8.97 nm and $\Delta\chi$=6.89°; (c) (85,34)@(77,55) with D=8.99 nm and $\Delta\chi$=8.40°; (d) (99,9)@(90,36) with D=8.80 nm and $\Delta\chi$=11.80°; (e) (99,11)@(86,43) with D=8.91 nm and $\Delta\chi$=13.90°; and (f) (72,48)@(105,15) with D=8.87 nm and $\Delta\chi$=16.83°.

To demonstrate the possibility of finding the same types of relative alignment (types I and II) for pairs of graphene walls of different chiralities, relative alignment maps analogous to those depicted in Fig. 2(a) were generated for a broad range of combinations of graphene walls; this included zigzag@chiral, armchair@chiral, and chiral@chiral DWCNTs for different diameters and different values of $\Delta\chi$. The CNT indices for the various pairs of walls were chosen to satisfy the constraint that the intertube spacing must be $\Delta r \sim 3.4$ Å (in this study, we used $\Delta r = 3.45 \pm 0.10$ Å). Relative alignment maps for different combinations of DWCNT indices are shown in Figs. 3–5. From these maps, it is evident that for a pair of graphene walls with a chiral-angle difference $\Delta\chi \neq 0$, the regions of atoms with the same intershell alignment type are finite in size and form clusters arranged in a periodic pattern throughout the nanotube. Figure 3 shows maps for pairs of chiral nanotubes with practically the same average diameter D and $\Delta\chi$ ranging from 3.88° to 16.8°. From the analysis of these maps, we conclude that the size of the clusters of atoms with the same type of relative alignment depends strongly on the value of $\Delta\chi$; specifically, the cluster size increases as $\Delta\chi$ decreases. Obviously, when $\Delta\chi \to 0$ (cases analyzed in Fig. 2), the resulting regions have an infinite size (i.e., limited by the actual CNT length).

Figure 4 shows that the size of these clusters does not change appreciably as the average DWCNT diameter increases. In conjunction with the results of Fig. 3, this trend implies that the size of the local intershell bonded structures is limited only by the chiral-angle difference $\Delta\chi$. Consequently, nanotubes of larger diameter are characterized by a larger number of clusters of atoms with certain alignment but not of larger size. Figure 5 demonstrates that the size of these clusters is independent of the individual chiral angles χ of the adjacent graphene walls; in summary, combining the results of Figs. 3–5 leads to the conclusion that the chiral-angle difference $\Delta\chi$ is the key parameter that determines the maximum size of the clusters with the same type of intershell alignment.

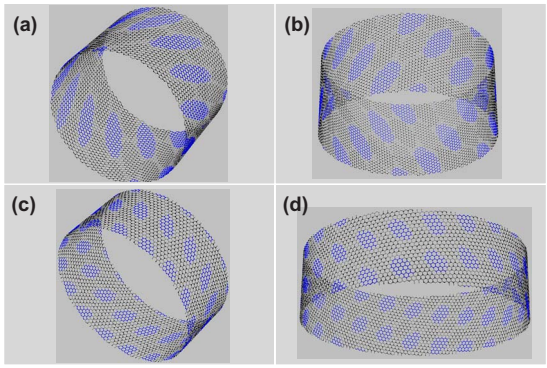

FIG. 4. (Color online) Relative alignment maps for DWCNTs with indices (a) (58,58)@(70,56) with D=8.56 nm and $\Delta\chi$=3.67°; (b) (94,94)@(110,88) with D=13.45 nm and $\Delta\chi$=3.67°; (c) (112,0)@(112,16) with D=9.46 nm and $\Delta\chi$=6.59°; and (d) (165,0)@(161,23) with D=13.59 nm and $\Delta\chi$=6.59°. Only the outer nanotubes are shown for clarity and the gray shading (coloring online) scheme is consistent with that of Fig. 3. Comparing (a) with (b) and (c) with (d) shows that the sizes of the gray shaded (colored online) regions are independent of the DWCNT average diameter and depend only on the difference in the chiral angle, $\Delta\chi$, of the two nanotubes in each DWCNT.

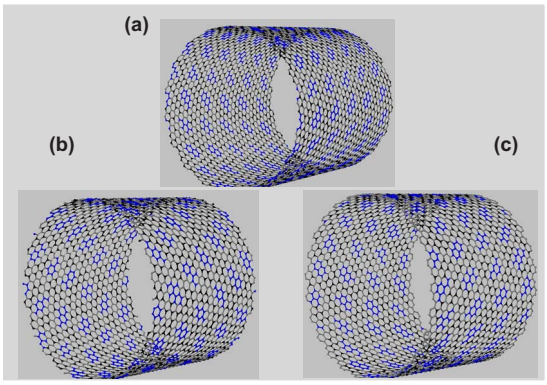

FIG. 5. (Color online) Relative alignment maps for DWCNTs with indices (a) (56,0)@(54,18) with D=5.08 nm and $\Delta\chi$=13.9°; (b) (31,31)@(50,20) with D=4.89 nm and $\Delta\chi$=13.9°; and (c) (54,6)@(50,25) with D=5.18 nm and $\Delta\chi$=13.9°. Only the outer nanotubes are shown for clarity and the gray shading (coloring online) scheme is consistent with that of Fig. 3. Comparing (a), (b), and (c) with each other shows that the sizes of the gray shaded (colored online) regions are independent of the chirality of the individual nanotubes and depend only on the difference in the chiral angle, $\Delta\chi$, of the two nanotubes in each DWCNT.

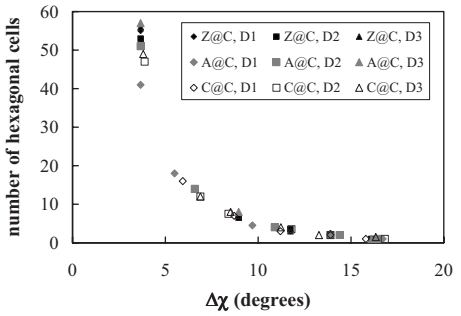

FIG. 6. Maximum number of hexagonal cells in an individual patch of a relative alignment map in DWCNTs as a function of the difference in the chiral angles, $\Delta\chi$, between the individual nanotubes of the DWCNTs and for various DWCNT average diameters. Black, gray, and open symbols are used to represent combinations of zigzag (Z) and chiral (C) walls (Z@C), armchair (A) and chiral walls (A@C), and two chiral walls (C@C), respectively. Diamonds, squares, and triangles correspond to DWCNTs with average external diameters $D_1=5.20$ nm, $D_2=9.01$ nm, and $D_3=13.64$ nm, respectively.

From the analysis of the maps of Fig. 3, it is evident that the size of the regions aligned according to the same type decreases abruptly as $\Delta\chi$ increases. Around a value of $\Delta\chi=16°$, the number of atoms in such a cluster decreases to six, i.e., enough to form just three intershell bonds such as those in the structures of Fig. 1. In order to quantify this trend, the dependence on the chiral-angle difference $\Delta\chi$ of the maximum size of clusters with type-II alignment [dark gray (blue online) regions] is plotted in Fig. 6. For all the DWCNT diameters examined, the cluster size is determined from the number of hexagonal cells in the regions under consideration. For each DWCNT, the size of the blue regions is the same as that of the black regions. This plot also emphasizes our previous conclusion that the sizes of the local intershell bonded structures, as measured by the size of same-alignment intershell clusters, are limited only by the chiral-angle difference $\Delta\chi$ of the adjacent graphene walls.

B. DFT analysis of intershell C-C bonding in MWCNTs

Our first-principles DFT analysis of intershell C-C bonding in pristine MWCNTs aims at providing insights and reaching quantitative conclusions regarding the formation of seed structures for the nucleation of nanocrystalline diamond phases. Here, we report representative results of our DFT analysis focusing on interactions between the concentric graphene walls of the triple-walled CNT (TWCNT) (6,0)@(15,0)@(24,0). In the structurally optimized configuration of this pristine TWCNT, the interwall distances between the (6,0) and (15,0), and the (15,0) and (24,0) nanotubes are equal to 3.4 Å. The results of the DFT analysis are shown in Figs. 7 and 8. The analysis confirms that specific alignments of concentric graphene walls result in the formation of intershell C-C bonds in MWCNTs that constitute the seed units for the nucleation of specific crystalline C phases. These specific alignments are consistent with those described in Sec. III A.

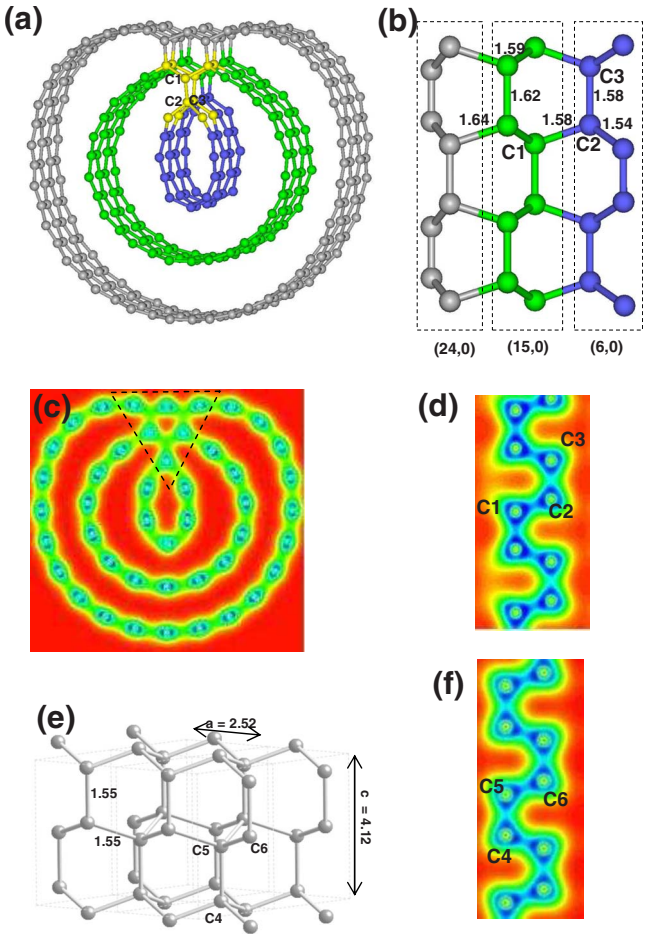

FIG. 7. (Color online) Structure resulting from intershell C-C bonding in a MWCNT according to first-principles DFT calculations. [(a)–(d)] Optimized atomic configuration of MWCNT with indices (6,0)@(15,0)@(24,0), i.e., with (6,0), (15,0), and (24,0) concentric inner [shaded very dark gray (colored in blue online)], middle [shaded dark gray (colored in green online)], and outer [shaded gray (colored in gray online)] nanotubes, respectively, depicting intershell C-C bonding. (a) Top view along the axial direction. (b) Cross-sectional view on the symmetry plane. Very dark gray (blue online), dark gray (green online), gray, and light gray (yellow online) spheres denote C atoms. The light-gray shaded (yellow-colored online) C atoms highlight the seed unit for the nucleation of a bulk phase of hexagonal diamond (lonsdaleite). (c) VED distribution on a plane perpendicular to the axial direction of the MWCNT. (d) VED distribution on a plane parallel to the axial direction of the MWCNT containing the atoms labeled C1, C2, and C3 in (a) and (b). The VED distributions in (c) and (d) highlight the intertube interactions and reveal the intershell C-C bonding and the accompanying shell distortions and structural relaxations [e.g., region enclosed by the triangle in (c)]. (e) Lonsdaleite lattice. (f) VED distribution for the lonsdaleite phase on the plane of C atoms labeled C4, C5, and C6 in (e). In (b) and (e), the numbers shown indicate interatomic distances or lattice parameters in Å. In (c), (d), and (f), the VED increases as the color changes from red (zero VED) to blue. For interpretation of the referneces to color in the VED distributions, the reader is referred to the online version of this article.

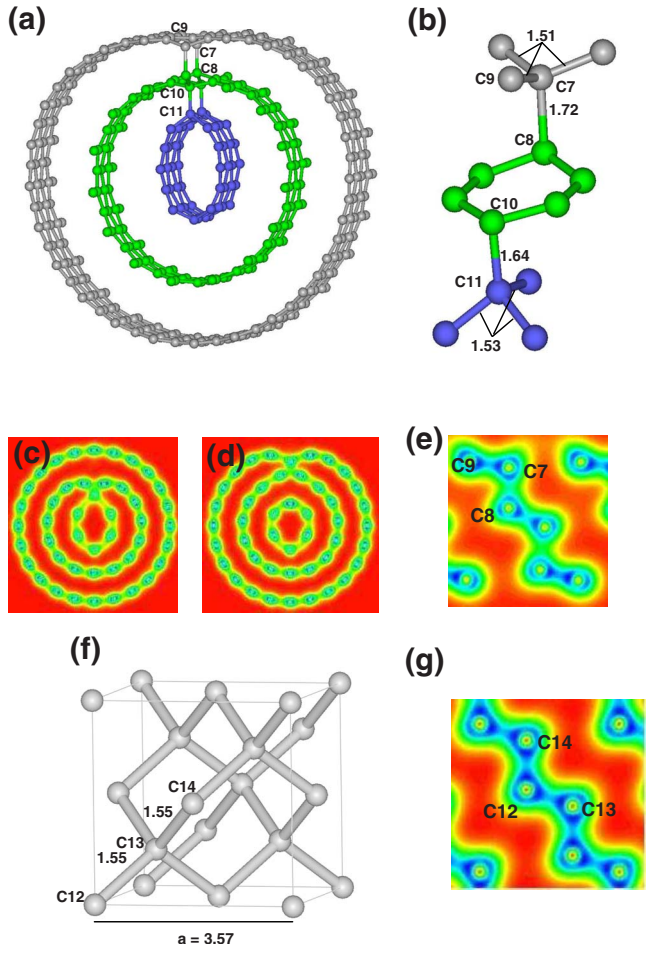

FIG. 8. (Color online) Structure resulting from intershell C-C bonding in a MWCNT according to first-principles DFT calculations. (a)–(e) Optimized atomic configuration of a (6,0)@(15,0)@(24,0) MWCNT with (6,0), (15,0), and (24,0) concentric inner [shaded very dark gray (colored in blue online)], middle [shaded dark gray (colored in green online)], and outer [shaded gray (colored in gray online)] nanotubes, respectively, depicting intershell C-C bonding. (a) Top view along the axial direction. (b) Only a small region from the original supercell in (a) is shown highlighting the seed unit for the nucleation of a cubic-diamond crystal. Very dark gray (blue online), dark gray (green online), and gray spheres denote C atoms. (c) VED distribution on a plane perpendicular to the axial direction of the MWCNT. (d) VED distribution on another plane perpendicular to the axial direction of the MWCNT. (e) VED distribution on a plane containing the atoms labeled C7, C8, and C9 in (a) and (b). The VED distributions in (c), (d), and (e) highlight the intertube interactions and reveal the intershell C-C bonding and the accompanying shell distortions and structural relaxations. (e) Cubic-diamond lattice. (f) VED distribution for the cubic-diamond phase on the plane of C atoms labeled C12, C13, and C14 in (f). In (b) and (f), the numbers shown indicate interatomic distances or lattice parameters in Å. In (c), (d), (e), and (g), the VED increases as the color changes from red (zero VED) to blue. For interpretation of the references to color in the VED distributions, the reader is referred to the online versiion of this article.

Figure 7 shows results of intershell C-C bonding in the TWCNT that may lead to the nucleation of the hexagonal-diamond phase; the atoms constituting the seed unit for the hexagonal-diamond phase nucleation are colored yellow in Fig. 7(a). In this case, the adjacent graphene walls of the (6,0) and (15,0) nanotubes are displaced with respect to each other in the axial direction by a distance equal to one half of the sp^2 C-C bond length, i.e., an alignment consistent with that of Fig. 1(c), and the graphene walls of the (6,0) and (24,0) nanotubes have overlapping hexagonal cells if projected onto the same plane normal to the radial direction, i.e., an alignment consistent with that of Fig. 1(b). The resulting intershell C-C bonding in this specific alignment leads to a structural configuration that resembles stacking of planes in a manner equivalent to the …*ABAB*… stacking in the hexagonal-diamond phase. Figures 7(a) and 7(b) depict intershell C-C bonds between the (6,0) and (15,0) nanotubes and between the (15,0) and (24,0) nanotubes; the presence of subsequent outer nanotubes may lead to the formation of a larger nanocrystal, as discussed in our MD studies of Sec. III C. The configuration depicted in Figs. 7(a) and 7(b) consists of six-member rings of C atoms due to the local tetrahedral geometries. The intershell interactions and the resulting local sp^3 bonding are highlighted by the valence electron-density (VED) distributions of Figs. 7(c) and 7(d); this bonding is characterized by an average bond length and bond angle of 1.56 Å and 109.31°, respectively. Evidence of strong intershell C-C bonding is provided by the shared electronic charge in the region enclosed by the dashed triangle in Fig. 7(c). Figure 7(e) shows the crystalline lattice of the bulk hexagonal-diamond phase (lonsdaleite); the corresponding electronic structure is depicted in the VED distribution of Fig. 7(f). The nearly identical local bonding environment shown in the VED distributions of Figs. 7(d) and 7(f), corresponding to the intershell bonded TWCNT and the bulk hexagonal-diamond phase, confirms the possibility of formation of hexagonal diamond as a result of intershell interactions leading to intershell C-C bonding in MWCNTs.

In a similar manner, Fig. 8 shows DFT results of intershell C-C bonding in the (6,0)@(15,0)@(24,0) TWCNT that may lead to the nucleation of the cubic-diamond phase. In this case, the adjacent graphene walls of the (6,0) and (15,0) nanotubes are displaced with respect to each other in the axial direction by a distance equal to one sp^2 C-C bond length and the graphene walls of the (15,0) and (24,0) nanotubes are further displaced by a distance equal to one sp^2 C-C bond length; as a result, the three carbon nanotubes have the relative alignment depicted in Fig. 1(a). The intershell C-C bonds between the adjacent graphene walls of the TWCNT are shown in Fig. 8(a) and in the close view of Fig. 8(b). The intershell C-C bonding in this specific alignment leads to a structural configuration that resembles stacking of planes in a manner equivalent to the …*ABCABC*… stacking in the cubic-diamond phase. The VED distributions in Figs. 8(c)–8(e) highlight the intershell interactions and the resulting local sp^3 bonding between the adjacent graphene walls of the TWCNT. In order to characterize the resulting crystalline phase of carbon that may be nucleated from this crosslinking of CNTs, we examine the close view of a small region, Fig. 8(b), from the original supercell shown in Fig. 8(a). The local (top) gray tetrahedral unit that is shown to have formed in Fig. 8(b) has an average bond length and bond angle of

1.56 Å and 109.33°, respectively, while the (bottom) tetrahedral unit shown in dark gray (blue online) has an average bond length and bond angle of 1.55 Å and 109.42°, respectively. This local structural unit that has formed from intershell interactions in the (6,0)@(15,0)@(24,0) TWCNT provides the seed unit for the nucleation of the cubic-diamond phase. The crystalline lattice of the bulk cubic-diamond phase is shown in Fig. 8(f). The similarities in the bonding environment of the seed unit of Figs. 8(a) and 8(b) with that of the bulk cubic-diamond phase, Fig. 8(f), are evident by comparing the VED distributions of Figs. 8(e) and 8(g). The VED distribution of Fig. 8(e) is in the plane of carbon atoms labeled C7, C8, and C9 in the TWCNT configuration of Fig. 8(a) while the VED distribution of Fig. 8(g) corresponds to the bulk cubic-diamond phase.

C. MD-generated structurally relaxed intershell bonded nanocrystalline structures embedded in MWCNTs

Our DFT analysis of Sec. III B examined the possibility of nucleation of crystalline diamond phases through intershell C-C bonding in a representative MWCNT configuration. Here, we explore further the nucleation and growth of such crystalline C phases over the broadest range of CNT geometrical parameters building on the geometrical findings of Sec. III A. Given our testing and validation of the AIREBO potential for this study in Sec. II, we generated structurally relaxed intershell bonded nanocrystalline structures based on MD computations with interatomic interactions described by the AIREBO potential. This AIREBO-MD-based structural relaxation procedure allowed for the computationally efficient exploration of the parameter space, including MWCNT configurations of sizes much larger than those that can be handled easily by first-principles DFT analysis.

Representative results of a systematic and comprehensive structural relaxation study of intershell bonded nanocrystalline structures embedded in DWCNTs are shown in Figs. 9–11. This study spanned a broad range of the parameter space discussed in Sec. III A. In each of the cases shown in Figs. 9–11, two regions of the DWCNT are chosen characterized by relative (intershell) alignments of type I and type II, respectively. To aid in the visualization of the resulting intershell bonded relaxed structures, we have used a local frame of reference appropriate for the structural analysis of each region and generated different planar views using the corresponding local coordinate system. In all cases in Figs. 9–11, consistent with the findings of Sec. III A, the relaxed intershell bonded structures in DWCNT regions of type-I and type-II alignment are nanocrystalline regions that can be viewed as seeds for the nucleation of the cubic-diamond and hexagonal-diamond phase, respectively.

The cases depicted in Figs. 9–11 correspond to DWCNTs of similar average diameter but different combinations of graphene wall configurations and different values of $\Delta\chi$. In Figs. 9–11, the graphene wall combinations are armchair@chiral, chiral@chiral, and zigzag@chiral, respectively; the specific DWCNT indices in Figs. 9–11 are (63,63)@(81,54), (99,9)@(90,36), and (110,0)@(95,38), respectively, and the corresponding $\Delta\chi$ values are 6.6°, 11.8°, and 16.1°. By comparing the configurations of Figs. 9–11, it is evident that their main difference is in the size of the

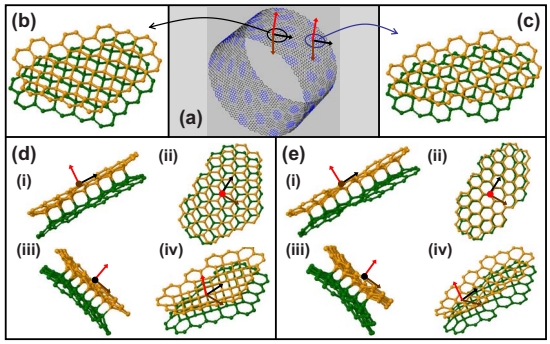

FIG. 9. (Color online) Representative MD-relaxed local structures formed by the creation of intershell C-C bonds in a DWCNT with indices (63,63)@(81,54) and $\Delta\chi$=6.6°. (a) Regions of the DWCNT where these relaxed structures are created, marked with black and blue circles, and local coordinate vectors used for structural analysis and visualization. Only the outer nanotube of the DWCNT is shown for clarity and the gray shading (coloring online) scheme is consistent with that of Fig. 3. [(b) and (c)] Local structures that can act as seeds for the nucleation of (b) the cubic-diamond phase and (c) the hexagonal-diamond phase, extracted from the DWCNT. [(d) and (e)] Different planar views, (i), (ii), (iii), and (iv), of the structures given in (b) and (c), respectively, using the local coordinates defined in (a). In (b)–(e), light and dark gray (orange and green online) spheres are used to represent carbon atoms belonging to the outer and inner nanotube of the DWCNT, respectively.

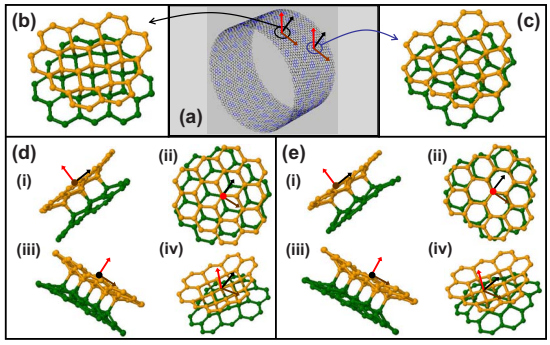

FIG. 10. (Color online) Representative MD-relaxed local structures formed by the creation of intershell C-C bonds in a DWCNT with indices (99,9)@(90,36) and $\Delta\chi$=11.8°. (a) Regions of the DWCNT where these relaxed structures are created, marked with black and blue circles, and local coordinate vectors used for structural analysis and visualization. Only the outer nanotube of the DWCNT is shown for clarity and the gray shading (coloring online) scheme is consistent with that of Fig. 3. [(b) and (c)] Local structures that can act as seeds for the nucleation of (b) the cubic-diamond phase and (c) the hexagonal-diamond phase, extracted from the DWCNT. [(d) and (e)] Different planar views, (i), (ii), (iii), and (iv), of the structures given in (b) and (c), respectively, using the local coordinates defined in (a). In (b)–(e), light and dark gray (orange and green online) spheres are used to represent carbon atoms belonging to the outer and inner nanotube of the DWCNT, respectively.

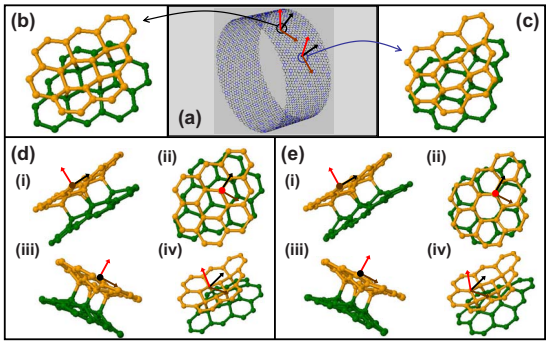

FIG. 11. (Color online) Representative MD-relaxed local structures formed by the creation of intershell C-C bonds in a DWCNT with indices (110,0)@(95,38) and $\Delta\chi=16.1°$. (a) Regions of the DWCNT where these relaxed structures are created, marked with black and blue circles, and local coordinate vectors used for structural analysis and visualization. Only the outer nanotube of the DWCNT is shown for clarity and the gray shading (coloring online) scheme is consistent with that of Fig. 3. [(b) and (c)] Local structures that can act as seeds for the nucleation of (b) the cubic-diamond phase and (c) the hexagonal-diamond phase, extracted from the DWCNT. [(d) and (e)] Different planar views, (i), (ii), (iii), and (iv), of the structures given in (b) and (c), respectively, using the local coordinates defined in (a). In (b)–(e), light and dark gray (orange and green online) spheres are used to represent carbon atoms belonging to the outer and inner nanotube of the DWCNT, respectively.

nanocrystals generated due to the intershell C-C bonding. Consistent with the results of Figs. 3–6, the resulting nanocrystal size decreases as the chiral-angle difference $\Delta\chi$ increases. Moreover, close inspection of the borders of these nanocrystalline regions shows the increased misalignment between the two graphene walls compared to their alignment inside the nanocrystalline regions; this confirms further the finite sizes expected of these seed units formed due to intershell C-C bonding between adjacent graphene walls of random chiral-angle combinations in MWCNTs.

In all the structurally relaxed intershell bonded nanostructures that we generated, we computed the energy difference, ΔE, between the original MWCNT and the resulting fully relaxed intershell bonded structures; the original MWCNT structure always corresponds to the lowest-energy state. In all cases, the results of this energetic analysis and their implications for thermodynamic stability are very similar; they are based on the quantity $\Delta E_B \equiv \Delta E / N_{\text{bonds}}$, where N_{bonds} is the number of intershell C-C bonds formed. This computation was carried out for both types of relative alignment resulting in cubic-diamond and hexagonal-diamond nanocrystals. The most important outcome of this computation is that the nanostructures with embedded cubic-diamond nanocrystals are always lower in energy, and therefore thermodynamically more stable, than those with embedded hexagonal-diamond nanocrystals. This is consistent with the difference between the cohesive energies of the corresponding bulk crystalline structures, as shown in Table I. Furthermore, for each MWCNT examined, the difference in ΔE_B between the two types of nanostructures (with embedded cubic-diamond vs hexagonal-diamond nanocrystals) is practically independent of the number of intershell C-C bonds, e.g., for the (50,50)@(55,55) DWCNT discussed in Sec. III A, $\Delta E_B = 0.32$ eV (according to AIREBO-MD relaxation) independent of N_{bonds}.

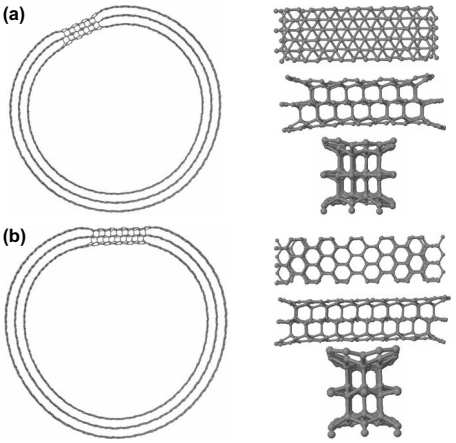

FIG. 12. Crystalline structures embedded locally in a (50,50)@(55,55)@(60,60) MWCNT due to intershell C-C bonding that provide seeds for the nucleation of (a) cubic diamond and (b) hexagonal diamond. In both (a) and (b), a top view of the MWCNT with the embedded nanocrystal is shown on the left and three different close planar views of the nanocrystalline regions are shown on the right, corresponding from top to bottom to the planes (θ,z), (r,θ), and (r,z) in a cylindrical-coordinate system.

Finally, Fig. 12 shows relaxed structures of nanocrystals embedded in a MWCNT with more graphene walls, namely, a TWCNT, to simply illustrate the growth in size of these nanocrystalline phases with the availability of multiple graphene walls for further intershell C-C bonding. For simplicity, an armchair@armchair@armchair nanotube is chosen, (50,50)@(55,55)@(60,60), and nanocrystals are generated by intershell C-C bonding in regions of type-I and type-II alignment depicted in Figs. 12(a) and 12(b), respectively, leading to a cubic-diamond and a hexagonal-diamond nanocrystal, respectively. Structural analysis, aided by the different close planar views of the nanocrystalline regions shown in Fig. 12, highlights the symmetries of the cubic-diamond and hexagonal-diamond phases in the central regions of the nanocrystals and how these symmetries are broken at the corresponding boundary regions.

IV. SUMMARY AND CONCLUSIONS

In summary, we presented a systematic analysis of the nanocrystalline structures that can be generated as a result of the intershell C-C bonding between adjacent concentric graphene walls of MWCNTs. Our analysis was based on a combination of important geometrical, chemical, and structural elements of MWCNTs. This included a comprehensive exploration of the corresponding geometrical parameter space as determined by the indices of the individual nanotubes that comprise the MWCNT, first-principles density-functional theory calculations of intershell C-C bonding between adjacent graphene walls in MWCNTs, and molecular-dynamics-based structural relaxation of the resulting

intershell bonded nanocrystalline structures employing a well validated interatomic potential. These structures can be viewed as nuclei for the growth of cubic-diamond and hexagonal-diamond nanocrystals embedded in the MWCNTs. We derived systematic rules for the determination of the lattice structure of the resulting nanocrystals according to the chirality and the relative alignment of adjacent graphene walls in the MWCNT. We demonstrated the formation of these crystalline phases over a broad range of nanotube diameters and for any possible combination of zigzag, armchair, or chiral configurations of graphene walls. Finally, we found that the size of the generated nanocrystals due to such intershell bonding depends strongly on the chiral-angle difference between adjacent graphene walls in the MWCNT.

Although the emphasis of this study is not on the origin of the intershell C-C bonding in MWCNTs, we believe that this may be possible due to a number of experimental circumstances including the interaction of H atoms with the MWCNT graphene walls or increased pressure and temperature in shock tubes. We have generated numerous pathways of H-induced intershell C-C bond formation based on first-principles DFT calculations in conjunction with the climbing-image-nudged elastic band method;[59] these results will be reported in a forthcoming publication. Here, we only mention that in the absence of H atoms, our DFT calculations revealed that the formation of the seed structure for nucleation of the lonsdaleite phase on a (6,0)@(15,0) DWCNT, i.e., the two inner tubes of the TWCNT of Fig. 7(a), required overcoming an activation energy barrier over 3.8 eV; this value corresponds to the energy difference between the original DWCNT and that containing intershell C-C bonds as shown in Fig. 7(a), which is the higher-energy state. This implies that in the absence of H atoms, nucleation of the lonsdaleite phase is kinetically prohibited over the temperature range reported in experiments.[24] The calculated activation barriers are generally high for nucleation of either cubic or hexagonal diamond over the range of MWCNT chiralities and adjacent graphene wall alignments that we examined. In brief, our first-principles calculations indicate that the formation of crystalline seeds for the nucleation of the lonsdaleite and cubic-diamond crystalline phases is induced by H-MWCNT interactions, consistent with experiments which reported that MWCNT transformations are observed exclusively due to their exposure to a hydrogen plasma.[24]

ACKNOWLEDGMENTS

This work was supported by the National Science Foundation under Grants No. CBET-0613501, No. CBET-0613629, and No. CMMI-0531171. One of the authors (A.R.M.) also acknowledges support through Fulbright/CAPES. Many fruitful discussions with Michael J. Behr and his editorial contributions on the initial draft of this paper are gratefully acknowledged.

*Corresponding author; maroudas@ecs.umass.edu

[1] C. Frondel and U. B. Marvin, Nature (London) **214**, 587 (1967).
[2] R. E. Hanneman, H. M. Strong, and F. P. Bundy, Science **155**, 995 (1967).
[3] H. W. Kroto, J. R. Heath, S. C. O'Brien, R. F. Curl, and R. E. Smalley, Nature (London) **318**, 162 (1985).
[4] S. Iijima, Nature (London) **354**, 56 (1991).
[5] S. S. Russell, C. T. Pillinger, J. W. Arden, M. R. Lee, and U. Ott, Science **256**, 206 (1992).
[6] R. S. Clarke, D. E. Appleman, and D. R. Ross, Nature (London) **291**, 396 (1981).
[7] H. Hirai and K. I. Kondo, Science **253**, 772 (1991).
[8] D. J. Erskine and W. J. Nellis, Nature (London) **349**, 317 (1991).
[9] F. Banhart and P. M. Ajayan, Nature (London) **382**, 433 (1996).
[10] M. Zaiser and F. Banhart, Phys. Rev. Lett. **79**, 3680 (1997).
[11] A. V. Krasheninnikov and F. Banhart, Nature Mater. **6**, 723 (2007).
[12] A. V. Palnichenko, A. M. Jonas, J.-C. Charlier, A. S. Aronin, and J.-P. Issi, Nature (London) **402**, 162 (1999).
[13] J. C. Angus and C. C. Hayman, Science **241**, 913 (1988).
[14] K. Fukunaga, J. I. Matsuda, K. Nagao, M. Miyamoto, and K. Ito, Nature (London) **328**, 141 (1987).
[15] F. P. Bundy and J. S. Kasper, J. Chem. Phys. **46**, 3437 (1967).
[16] H. Vora and T. J. Moravec, J. Appl. Phys. **52**, 6151 (1981).
[17] T. Singh, M. J. Behr, E. S. Aydil, and D. Maroudas, Chem. Phys. Lett. **474**, 168 (2009).
[18] J. M. Cowley, R. C. Mani, M. K. Sunkara, M. O'Keefe, and C. Bonneau, Chem. Mater. **16**, 4905 (2004).
[19] B. Wen, J. J. Zhao, and T. J. Li, Int. Mater. Rev. **52**, 131 (2007).
[20] W. R. L. Lambrecht, C. H. Lee, B. Segall, J. C. Angus, Z. D. Li, and M. Sunkara, Nature (London) **364**, 607 (1993).
[21] N. Layadi, P. Roca i Cabarrocas, B. Drevillon, and I. Solomon, Phys. Rev. B **52**, 5136 (1995).
[22] S. Sriraman, S. Agarwal, E. S. Aydil, and D. Maroudas, Nature (London) **418**, 62 (2002).
[23] S. Sriraman, M. S. Valipa, E. S. Aydil, and D. Maroudas, J. Appl. Phys. **100**, 053514 (2006); M. S. Valipa, S. Sriraman, E. S. Aydil, and D. Maroudas, *ibid.* **100**, 053515 (2006).
[24] L. T. Sun, J. L. Gong, Z. Y. Zhu, D. Z. Zhu, S. X. He, Z. X. Wang, Y. Chen, and G. Hu, Appl. Phys. Lett. **84**, 2901 (2004).
[25] B. Wen, J. J. Zhao, T. J. Li, C. Dong, and J. Z. Jin, J. Phys.: Condens. Matter **17**, L513 (2005).
[26] A. S. Barnard, M. L. Terranova, and M. Rossi, Chem. Mater. **17**, 527 (2005).
[27] B. Peng, M. Locascio, P. Zapol, S. Y. Li, S. L. Mielke, G. C. Schatz, and H. D. Espinosa, Nat. Nanotechnol. **3**, 626 (2008).
[28] E. M. Byrne, M. A. McCarthy, Z. Xia, and W. A. Curtin, Phys. Rev. Lett. **103**, 045502 (2009).
[29] P. Badziag, W. S. Veowoerd, W. P. Ellis, and N. R. Greiner, Nature (London) **343**, 244 (1990).
[30] N. M. Hwang, J. H. Hahn, and D. Y. Yoon, J. Cryst. Growth **160**, 87 (1996).
[31] Q. Jiang, J. C. Li, and G. Wilde, J. Phys.: Condens. Matter **12**, 5623 (2000).

[32] A. S. Barnard, S. P. Russo, and I. K. Snook, J. Chem. Phys. **118**, 5094 (2003).
[33] M. Menon, E. Richter, P. Raghavan, and K. Teranishi, Superlattices Microstruct. **27**, 577 (2000).
[34] O. Shenderova, D. Brenner, and R. S. Ruoff, Nano Lett. **3**, 805 (2003).
[35] A. S. Barnard, S. P. Russo, and I. K. Snook, Nano Lett. **3**, 1323 (2003).
[36] A. S. Barnard and I. K. Snook, J. Chem. Phys. **120**, 3817 (2004).
[37] V. V. Ivanovskaya and A. L. Ivanovskii, Inorg. Mater. **43**, 349 (2007).
[38] M. S. Dresselhaus, Annu. Rev. Mater. Sci. **27**, 1 (1997).
[39] P. Hohenberg and W. Kohn, Phys. Rev. **136**, B864 (1964).
[40] W. Kohn and L. J. Sham, Phys. Rev. **140**, A1133 (1965).
[41] J. P. Perdew, K. Burke, and M. Ernzerhof, Phys. Rev. Lett. **77**, 3865 (1996).
[42] D. Vanderbilt, Phys. Rev. B **41**, 7892 (1990).
[43] M. C. Payne, M. P. Teter, D. C. Allan, T. A. Arias, and J. D. Joannopoulos, Rev. Mod. Phys. **64**, 1045 (1992).
[44] G. Kresse and J. Furthmuller, Phys. Rev. B **54**, 11169 (1996).
[45] H. J. Monkhorst and J. D. Pack, Phys. Rev. B **13**, 5188 (1976).
[46] S. J. Stuart, A. B. Tutein, and J. A. Harrison, J. Chem. Phys. **112**, 6472 (2000).
[47] D. W. Brenner, Phys. Rev. B **42**, 9458 (1990).
[48] D. W. Brenner, O. A. Shenderova, J. A. Harrison, S. J. Stuart, B. Ni, and S. B. Sinnott, J. Phys.: Condens. Matter **14**, 783 (2002).
[49] B. Ni, S. B. Sinnott, P. T. Mikulski, and J. A. Harrison, Phys. Rev. Lett. **88**, 205505 (2002).
[50] H. J. C. Berendsen, J. P. M. Postma, W. F. Vangunsteren, A. Dinola, and J. R. Haak, J. Chem. Phys. **81**, 3684 (1984).
[51] O. Gulseren, T. Yildirim, and S. Ciraci, Phys. Rev. Lett. **87**, 116802 (2001).
[52] A. R. Muniz, T. Singh, and D. Maroudas, Appl. Phys. Lett. **94**, 103108 (2009).
[53] R. H. Telling, C. P. Ewels, A. A. El-Barbary, and M. I. Heggie, Nature Mater. **2**, 333 (2003).
[54] A. Hashimoto, K. Suenaga, K. Urita, T. Shimada, T. Sugai, S. Bandow, H. Shinohara, and S. Iijima, Phys. Rev. Lett. **94**, 045504 (2005).
[55] M. Kuwabara, D. R. Clarke, and D. A. Smith, Appl. Phys. Lett. **56**, 2396 (1990).
[56] J. Xhie, K. Sattler, M. Ge, and N. Venkateswaran, Phys. Rev. B **47**, 15835 (1993).
[57] Z. Y. Rong and P. Kuiper, Phys. Rev. B **48**, 17427 (1993).
[58] W.-T. Pong and C. Durkan, J. Phys. D: Appl. Phys. **38**, R329 (2005).
[59] G. Henkelman, B. P. Uberuaga, and H. Jonsson, J. Chem. Phys. **113**, 9901 (2000).